

**Key Points:**

- We analyzed the composition of the Chang'E-5 landing zone using Lunar Mineralogical Spectrometer data
- Our results showed that the minerals near the landing site are mainly a mixture of two types of clinopyroxene and plagioclase
- The exotic materials in the Chang'E-5 region primarily originate from the Harpalus and Aristarchus craters

**Supporting Information:**

Supporting Information may be found in the online version of this article.

**Correspondence to:**

J. Huang,  
[junhuang@cug.edu.cn](mailto:junhuang@cug.edu.cn)





**Citation:**

Yang (杨茂升), M., Qian (钱煜奇), Y., Horgan, B., Huang (黄俊), J., & Xiao (肖龙), L. (2023). Mineralogy of surface materials at the Chang'E-5 landing site and possible exotic sources from in situ spectral observations. *Journal of Geophysical Research: Planets*, 128, e2023JE007908. <https://doi.org/10.1029/2023JE007908>

Received 18 MAY 2023

Accepted 6 OCT 2023

## Mineralogy of Surface Materials at the Chang'E-5 Landing Site and Possible Exotic Sources From In Situ Spectral Observations

Maosheng Yang (杨茂升)<sup>1</sup> , Yuqi Qian (钱煜奇)<sup>1</sup>, Briony Horgan<sup>2</sup> , Jun Huang (黄俊)<sup>1,3</sup> , and Long Xiao (肖龙)<sup>1,3</sup> 

<sup>1</sup>State Key Laboratory of Geological Processes and Mineral Resources, School of Earth Sciences, Planetary Science Institute, China University of Geosciences, Wuhan, China, <sup>2</sup>Department of Earth, Atmospheric and Planetary Sciences, Purdue University, West Lafayette, IN, USA, <sup>3</sup>Chinese Academy of Sciences Center for Excellence in Comparative Planetology, Hefei, China

**Abstract** China's Chang'E-5 (CE-5) mission landed at 43.06°N and 51.92°W on 1 December 2020, within the Northern Oceanus Procellarum region of the Moon. The CE-5 landing site is situated within a young lunar basalt unit estimated to be around 2.0 Ga. A comprehensive understanding of the lunar regolith composition within the CE-5 region is pivotal as it furnishes additional scientific evidence concerning its origin. This, in turn, would further improve our understanding of lunar geology and evolution. In our studies, we employed a variety of spectral data and derived products including the CE-5 Lunar Mineralogical Spectrometer data, the ferrous mineral abundance derived from Kaguya Multiband Imager, and the Chandrayaan-1 Moon Mineralogical Mapper data. These data enabled us to determine and analyze the compositions of the diverse materials present in the CE-5 region and to pinpoint the origins of exotic materials found therein. Our results indicated that the exotic material within the CE-5 region is principally composed of clinopyroxene and plagioclase (Pl). Further analysis unveils that the CE-5 regolith embodies a blend of two distinct varieties of clinopyroxene, designated as Type A and Type B, along with feldspar. This discovery markedly diverges from the conclusions drawn by preceding studies, which relied solely on remote sensing data. Moreover, the exotic materials are predominantly constituted by the ejecta of Harpalus and Aristarchus craters. This finding furnishes a substantial geological background for the analysis of exotic materials in the samples returned by the CE-5 mission in forthcoming studies.

**Plain Language Summary** China's Chang'E-5 (CE-5) mission successfully landed on the Moon within a young basalt unit. Understanding the composition of the lunar soil in this region is imperative for propelling our comprehension of lunar geology and its origin. Our analysis revealed that the lunar soil within the CE-5 region is an amalgam of three distinct mineral types. This finding challenges the previous understanding, which was primarily predicated on remote sensing data. Moreover, our investigation unearthed that the exotic materials found in the region primarily originate from the Harpalus and Aristarchus craters. This study endeavor furnishes novel insights regarding the provenance of exotic materials in the returned samples, thereby laying a substantial foundation for the ensuing examination of the CE-5 samples.

### 1. Introduction

On 1 December 2020, China's Chang'E-5 (CE-5) spacecraft landed at 43.06°N and 51.92°W (Wang et al., 2021) within the Northern Oceanus Procellarum (Figure 1). This mission marks the most recent robotic lunar sample return since Luna-24 in 1976. The landing site is located in one of the youngest lunar basalt fields (Qian, Xiao, Wang, et al., 2021) with an age of ~2.0 Ga (Che et al., 2021; Li et al., 2021). Subsequent analysis of the returned samples indicates that the CE-5 lunar soils predominantly consist of plagioclase and clinopyroxene, with minimal trace amounts of olivine and other minerals (Li et al., 2022). The lunar soils at the CE-5 landing site embody a blend of both local and exotic components. Previous studies have indicated that the majority of the returned samples originate from local basalts (He et al., 2022; Li et al., 2022), specifically the Em4 mare unit (Qian, Xiao, Head, et al., 2021; Qian et al., 2018). The Em4 unit (or named P58) is the Eratosthenian-aged moderate-Ti mare basalts (1.6–1.7 Ga) (Hiesinger, 2003; Qian et al., 2018). However, the presence of small quantities of exotic clasts (Zeng et al., 2023) and glass (Yang et al., 2022), characterized by compositions distinctly divergent from

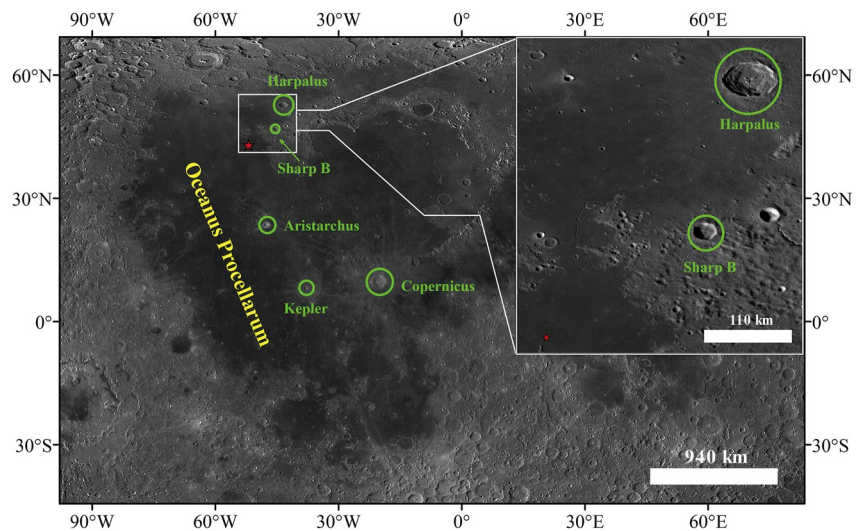


**Figure 1.** The CE-5 landing site is located at 43.06°N and 51.92°W (red star), while Aristarchus, Kepler, Copernicus, Harpalus, and Sharp B craters (green circles) are candidate sources of exotic ejecta. The basemap is the Chang'E-1 global mosaic, which can be accessed at [planets.cug.edu.cn](http://planets.cug.edu.cn)

the local materials, has also been discerned within the returned samples. The CE-5 exotic material may have been transported to the landing site from distant impact craters located outside the Em4 unit (Hou et al., 2022; Jia et al., 2021; Qian, Xiao, Wang, et al., 2021; Xie, Xiao, et al., 2020). Nonetheless, a consensus regarding the relative contribution of the candidate source craters remains elusive.

Xie, Xiao, et al. (2020) were the first to utilize a new ballistic sedimentation model to analyze the origin of exotic materials within the landing region. According to their findings, the volumetric abundance of the exotic material in the CE-5 regolith ranges approximately between 12% and 20%, with the Aristarchus crater contributing around 7% and the Pythagoras crater about 5% as the primary sources. Subsequently, Qian, Xiao, Wang, et al. (2021) also leveraging this model in their analysis, propose an alternative perspective. They posited that the predominant ejecta, categorized based on a morphologically-defined age classification, originates from the Harpalus crater, exhibiting a NE-SW orientation. Conversely, Jia et al. (2021) proposed that the NE-SW orientated ejecta derived from Sharp B crater, rather than Harpalus crater. Hou et al. (2022) re-determined the ages of all exotic source craters based on previous studies employing the crater size frequency distribution (CFSD) method. They proposed that Aristarchus, Copernicus, Harpalus, Kepler, and Sharp B craters are relatively younger than the CE-5 landing region, suggesting that these craters (green circles in Figure 1) could plausibly serve as the principal sources of the exotics at the CE-5 landing site. However, it is noteworthy that none of these studies delved into the composition of the CE-5 landing area and the exotic craters. In this study, building upon the five candidate craters delineated by Hou et al. (2022), we analyzed the material compositions to ascertain the more likely potential sources of exotic material within these five craters.

A profound comprehension of the lunar regolith composition within the CE-5 region will help provide additional scientific evidence regarding its origin, which, in turn, would further improve our understanding of lunar geology and dynamic processes. Such understanding can be achieved by analyzing the composition of in situ materials, exotic materials, and regolith materials present within the landing area. In this study, we utilized the in situ spectral measurements collected by the Lunar Mineralogical Spectrometer (LMS) aboard the Chang'E-5 lander, in conjunction with orbital spectral data, to investigate the source craters of the exotic materials.

## 2. Spectral Characteristics of Typical Lunar Minerals

Typical materials constituting the lunar surface encompass plagioclase, pyroxene, olivine, ilmenite, glass, and other minor minerals (Papike et al., 1991). The CE-5 returned samples primarily contain plagioclase and pyroxene as the main minerals (Li et al., 2022).

Olivine (Ol) exhibits a broad and asymmetric absorption band near 1.05  $\mu\text{m}$ , yet it lacks a 2  $\mu\text{m}$  absorption band (Cloutis & Gaffey, 1991; King & Ridley, 1987; Sunshine & Pieters, 1998). The spectral characteristics of pyroxene

are more varied. Pyroxenes (PX) can be broadly classified into two main types based on the differential amount of calcium present: orthopyroxenes and clinopyroxenes. Orthopyroxene (OPX) displays a relatively narrow and symmetrical absorption band near 0.9  $\mu\text{m}$ , alongside a broad absorption band near 1.9  $\mu\text{m}$  (Adams, 1975; Cloutis & Gaffey, 1991). In contrast, clinopyroxene (CPX) can be categorized into two spectral types: Type A CPX and Type B CPX. Type A CPX refers to high-Ca clinopyroxene, which exhibits a complex absorption band near 1  $\mu\text{m}$  yet lacks a 2  $\mu\text{m}$  absorption band, akin to Ol (Cloutis & Gaffey, 1991; Schade et al., 2004). Conversely, Type B CPX spectrally corresponds to low-Ca clinopyroxene, exhibits a narrow, symmetrical 1  $\mu\text{m}$  absorption band centered between 0.95 and 1.05  $\mu\text{m}$ , as well as a broad 2  $\mu\text{m}$  absorption band centered between 2.1 and 2.32  $\mu\text{m}$  (Adams, 1975; Cloutis & Gaffey, 1991). The distinctive spectral features of Type A CPX arise from the filling of the M2 site with  $\text{Ca}^{2+}$  ions (Cloutis & Gaffey, 1991; Klima et al., 2011; Warren & Lawrence Bragg, 1929). When the Wollastonite ( $\text{Ca}_2\text{Si}_2\text{O}_6$ , or Wo) content is high (as observed in certain diopside, hedenbergite, and augite compositions), the spectral features of Type B CPX transform into those characteristic of Type A CPX (Klima et al., 2011).

Certain variants of plagioclase (Pl) exhibit a broad absorption band centered between 1.10 and 1.35  $\mu\text{m}$  when  $\text{Fe}^{2+}$  substitutes for Ca, although this band is typically quite weak (Adams & Goullaud, 1978; Cloutis & Gaffey, 1991).

### 3. Data and Methods

#### 3.1. CE-5 Lunar Mineralogical Spectrometer Hyperspectral Data

The Lunar Mineralogical Spectrometer (LMS) constitutes one of the scientific payloads aboard the CE-5 lander (Zhou et al., 2022). It covers a spectral range from 480 to 3,200 nm, encompassing four distinct channels: visible (VIS; 480–950 nm), near-infrared (NIR; 900–1,450 nm), shortwave infrared (SWIR; 1,400–2,300 nm), and mid-wave infrared (MWIR; 2,200–3,200 nm) (Xu et al., 2022). The spectral resolution varies from 2.4 to 24.8 nm (Zhou et al., 2022).

LMS has two in-flight operation modes: (a) the full-band target mode (hyperspectral mode) and (b) the full-view scanning mode (multispectral mode) (Xu et al., 2022). The multispectral mode covers the entire sampling region, whereas the hyperspectral mode collects only a limited number of hyperspectral spectra in a region of interest. The data utilized in this study were acquired in the full-band target mode.

In this paper, the LMS spectral data covering the range of 480–2,650 nm were utilized to analyze the in situ spectra of CE-5. The VIS, NIR, and SWIR data were employed to delve into the mineralogy (Lv et al., 2022). A segment of the MWIR range (2,655–3,200 nm) was omitted from the analysis due to thermal effects (Lin et al., 2021). Beyond the 2,000 nm threshold, thermal emissions progressively dominate the signal, overpowering the near-infrared reflectance signals (Clark et al., 2011). The level 2B data of LMS were used in this study, which have gone through dark current subtraction, scattering-background correction, flat field, instrument temperature correction, radiometric calibration, and geometric calibration (J. J. Liu et al., 2022). The spectra were calibrated with respect to relative reflectance using solar irradiance (Gueymard, 2004) as per the methodologies delineated by Zhang et al. (2015) and Huang et al. (2020). Reflectance expressed in terms of the reflectance factor (Hapke, 2012) was obtained by using the solar irradiance calibration method (Zhang et al., 2015). Spectra derived from different detectors were merged by scaling at overlapping wavelengths to accommodate their varying responses. While the MWIR data remained unscaled, the SWIR, NIR, and VIS data were connected and scaled to the longer wavelength data (Figure 2). Due to data anomalies within the 940–950 nm range, the problematic bands in the merged scaled VIS spectra (Figure 2) were excised from the analysis.

#### 3.2. Kaguya Ferrous Mineral Abundance Mosaic

The Multiband Imager (MI) is one of the 14 instruments on the Kaguya mission (Ohtake et al., 2008). The MI is a high-resolution multiband imaging camera that encompasses nine spectral bands in the VIS and NIR ranges (Kodama et al., 2010). Utilizing these multispectral images, nine near-global maps have been derived, including olivine, clinopyroxene, orthopyroxene, plagioclase, FeO, optical maturity, the abundance of SMFe, and the grain size for plagioclase (Lemelin et al., 2015, 2019). The derivation of these maps were derived employed Hapke's radiative transfer equations and the optical constants of Lucey et al. (2000), which were further refined by Lucey et al. (2014) (Lemelin et al., 2015, 2019). Validation of the method using spectra of lunar soil of known composition reveals an error in the mineral abundance estimation of  $\pm 8$  wt.% (Lemelin et al., 2015).

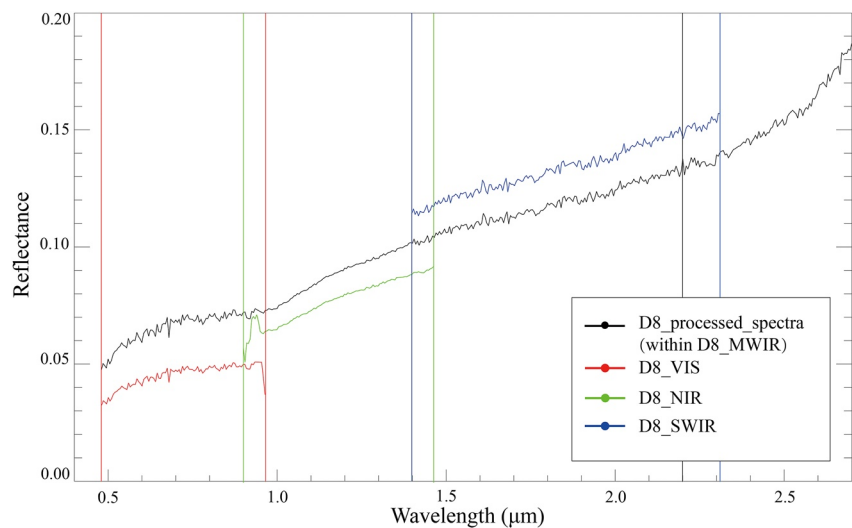


**Figure 2.** An example (D8) of the original and the processed LMS spectra. The black line represents the merged spectra scaled to the MWIR region. The red, green, and blue lines represent the original VIS data, original NIR data and original SWIR data, respectively. The vertical lines represent the spectral ranges of each spectrum.

In this study, where the discussion encompasses Type A CPX, it is pertinent to note that the CPX abundance is computed as the aggregate of a fraction of Type A CPX and the entirety of Type B CPX. Similarly, the olivine abundance is determined as the sum of a portion of Type A CPX and all olivine, based on Lemelin et al. (2015, 2019).

While the ferrous minerals weight percentage of derived from the MI may not reflect the ground truth weight percentage, it retains its utility in discerning the relative mineral content, chiefly the relative abundance of Orthopyroxene (OPX). Initially, we utilized the four mineral maps (olivine, clinopyroxene, orthopyroxene, and plagioclase) of the four candidate source craters (Aristarchus, Kepler, Copernicus, and Sharp B) and CE-5 landing region produced by Lemelin et al. (2019) to investigate candidate exotic material sources for the landing site.

While the ferrous mineral weight percentage ascertained from the Multiband Imager (MI) may not reflect the precise ground truth weight percentage, it retains its utility in discerning the relative mineral content, chiefly the relative abundance of Orthopyroxene (OPX). Initially, we employed a quartet of mineral maps encompassing Olivine, Clinopyroxene, Orthopyroxene, and Plagioclase of the four prospective source craters (Aristarchus, Kepler, Copernicus, and Sharp B) alongside the CE-5 landing vicinity, as delineated by Lemelin et al. (2019), to probe into the plausible exotic material origins for the landing site.

### 3.3. Moon Mineralogy Mapper Data

The Moon Mineralogy Mapper (M3) is a high-resolution, high-precision imaging spectrometer on Chandrayaan-1, with a spatial resolution of 140 m/pixel and 86 spectral bands spanning from 430 to 3,000 nm (Pieters et al., 2009). The M3's level 2 reflectance data, which were downloaded from the NASA Planetary Data System, has been subjected to several corrections, including radiometric correction (Green et al., 2011) geometric correction (Boardman et al., 2011), thermal correction (Clark et al., 2011), photometric correction (Besse et al., 2011; Hicks et al., 2011), and ground truth correction (Isaacson et al., 2013). This data is used as an integral part of our study.

As previously articulated, the categorization of Type A clinopyroxene (CPX), Type B CPX, and olivine predicated based on the MI-derived ferrous mineral weight is a challenge. To delve deeper into the intricacies of the material composition within the region, we collected hyperspectral M3 data of the potential source craters following the analysis predicated on MI. The M3 data were obtained at equidistant points from the center of the craters toward the landing site. The spectra of the Aristarchus and Harpalus craters were extracted from the M3 images M3G20090418T132620 (OP2A) and M3G20090209T033051 (OP1B), respectively.

### 3.4. Spectral Band Parameters

We utilize several band parameters devised by Horgan et al. (2014) that are sensitive to lunar mineralogy to quantitatively characterize the spectral features. The calculation of the band parameters requires the processing of the



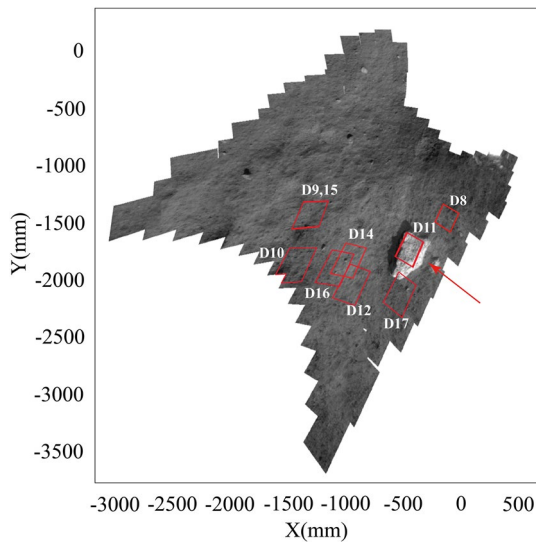


**Figure 3.** A diagram of the Lunar Mineralogical Spectrometer (LMS) working area. The red squares represent the footprints of the measurements of the LMS hyperspectral mode. The red arrow indicates the rock observed by the LMS instrument.

original spectra into continuum removed spectra. We removed the continuum of the LMS and M3 spectrum by fitting a second-order polynomial convex. The tie points adjusted to the maximize band area near 0.7, 1.5, and 2.5  $\mu\text{m}$ . The parameters we utilize in this manuscript include the band center, asymmetry, and band Area Ratio for the 1 and 2  $\mu\text{m}$  iron bands. The 1  $\mu\text{m}$  center (B1cen) represents the wavelength position within a 75 nm range around the band minimum in the 1  $\mu\text{m}$  absorption band. It is determined by fitting a fourth-order polynomial to all channels and finding the minimum. Similarly, the 2  $\mu\text{m}$  center (B2cen) represents the wavelength position within a 75 nm range around the band minimum in the 2  $\mu\text{m}$  absorption band. It also involves fitting a fourth-order polynomial to all channels but differs from B1cen in being focused on the 2  $\mu\text{m}$  band. The percentage of the total area corresponds to the 1  $\mu\text{m}$  asymmetry (B1asy), which is calculated as the difference between the band area to the left and right of B1cen. The area ratio is the ratio of the 2  $\mu\text{m}$  area to the 1  $\mu\text{m}$  area. The area is calculated by subtracting the value of each channel in the given range from one (1) and then multiplying it by the spectral resolution at that channel. These parameters are typically plotted in combinations, such as band center versus asymmetry for the 1  $\mu\text{m}$  band, 1 versus 2  $\mu\text{m}$  band centers, and 1  $\mu\text{m}$  band centers versus band Area Ratio.

## 4. Results

### 4.1. CE-5 Landing Site

The CE-5 landing site is located within the Em4 unit in the Northern Oceanus Procellarum (Qian et al., 2018). The Em4 unit is a young and relatively flat mare unit. This study encompasses the analysis of nine spectra acquired by the CE-5 Lunar Mineralogical Spectrometer (LMS), designated as D8, D9, D10, D11, D12, D14, D15, D16, and D17, respectively. The spatial distribution of these spectra is illustrated in Figure 3. It merits mention that the LMS hyperspectral data coverage encompasses a relatively small area of approximately  $3 \times 3 \text{ m}^2$  in proximity to the landing site. The spectra were sampled from the lunar soil, with the exception of D11, which was sampled on a rock near the landing area (Figure 3).

All of the spectra exhibit a significant red slope in the VIS and NIR band due to space weathering (Pieters, Taylor, Noble, et al., 2000). For the soil spectra (D8, D9, D10, D12, D14, D15, D16, and D17), the B1cen values range from 0.97 to 1.03  $\mu\text{m}$ , the B1asy values range from 0.15 to 0.35, and the B2cen values range from 1.97 to 2.15  $\mu\text{m}$ . Additionally, the Area Ratio ranges from 0.24 to 0.52. Based on the three combination diagrams of the band parameters, the soil spectra can be divided into three distinct groups. The first group is characterized by lower B1cen, higher B1asy, higher B2cen, and lower Area Ratio (such as D12) compared to all the LMS spectra. The second group shows a higher B1cen, lower B1asy, lower B2cen, and higher Area Ratio (like D14 and D15). The residual samples can be deemed transitional between the two initial groups (Figures 4c–4e). D11 represents the only spectra obtained from lunar rock. The spectra of D11 exhibit more prominent 1 and 2  $\mu\text{m}$  spectral features than the other soil spectra (Figure 4a). The band parameters of D11 are similar to those of D12, with B1cen at 0.97  $\mu\text{m}$ , B1asy at 0.46, B2cen at 2.11  $\mu\text{m}$ , and an Area Ratio of 0.23.

According to the Kaguya MI ferrous mineral abundances, the absolute mineral abundances of CPX, OPX, OI, and Pl (Lemelin et al., 2015, 2019) are estimated surrounding the CE-5 site. We discerned two kinds of vertical striping within the study area (depicted as yellow and purple unit in Figure 5). We believe that the yellow unit is more plausible and the center of the landing zone is also located on the yellow unit. It has an CPX  $\sim 37 \text{ wt.}\%$ , OPX  $\sim 9 \text{ wt.}\%$ , OI  $\sim 14 \text{ wt.}\%$  and Pl  $\sim 40 \text{ wt.}\%$ , assuming CPX + OPX + OI + Pl = 100 wt.% (white square in Figure 5). The abundances of CPX and Pl are high and OI and OPX are low.

### 4.2. Candidate Source Craters of the Ejecta in CE-5 Landing Site

The composition of ejecta can exhibit significantly in different directions due to factors such as impact angle, velocity, target composition, and topography (Collins et al., 2012; Melosh, 1989). In scrutinizing the composition of candidate exotic materials at the landing site, the relative position of the impact crater in relation to the landing

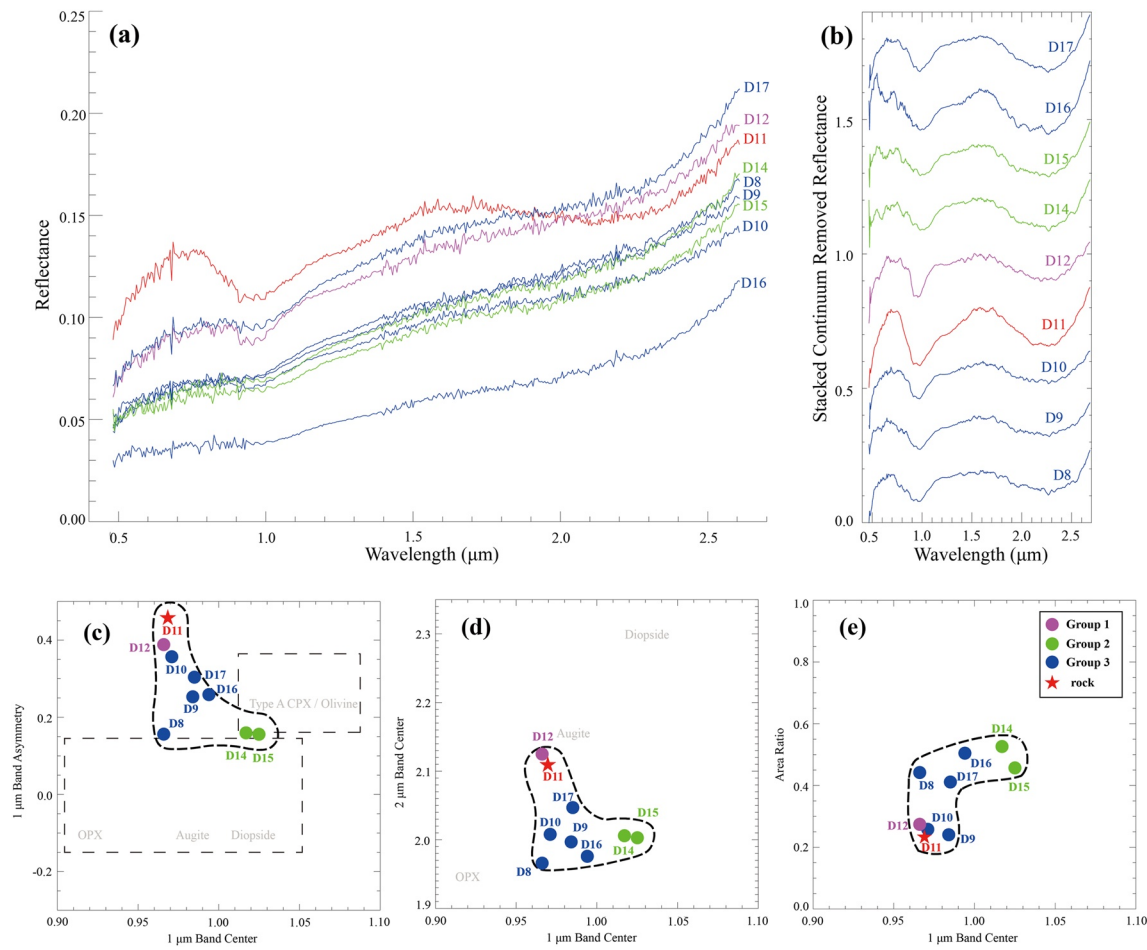


**Figure 4.** Lunar Mineralogical Spectrometer (LMS) hyperspectral data. (a) Reflectance of the processed spectra. (b) Continuum-removed reflectance. (c–e) Comparison of 1 and 2 μm band parameters for the CE-5 LMS data. The purple, green, and blue points represent the soil spectrum of Group 1, Group 2, and Group 3, respectively. The red star represents the rock's spectra (D11). Specific sample information is listed in Table S1 in Supporting Information S1.

site must be considered. For the Aristarchus, Kepler, and Copernicus craters, their northern ejecta is oriented toward the CE-5 landing site, whereas for the Harpalus and Sharp B craters, their southwest ejecta is directed toward the CE-5 site (Figure 1). Additionally, the thickness of the ejecta augments in proximity to the crater rim (Collins et al., 2012; Xie, Liu, & Xu, 2020). The more pronounced the ejecta thickness, the more discernible the spectral characteristics of the ejecta minerals compared to the background. The material ejected from the impact crater retains the same orientation, relative to the center of the impact crater, as the pre-impact material (Collins et al., 2012; Xie, Liu, & Xu, 2020). Hence, we selected spectra from the corresponding directions near the rim of the ejecta and their background for the analysis of spectral properties and composition of any candidate exotic materials from these five craters.

#### 4.2.1. Kepler

Kepler crater is located at 8.11°N and 38°W, southeast of the landing site, and has a diameter of 30.12 km. The study area for this crater spans between 3.5 and 12°N and 34–42.5°W (Figure 6a). The crater is positioned between Mare Insularum and Oceanus Procellarum. We selected spectra corresponding to two ejecta blankets and Oceanus Procellarum basalts. The absolute mineral abundances of the nearby ejecta unit are CPX ~ 19 wt.%, OPX ~ 24 wt.%, Ol ~ 4 wt.% and Pl ~ 53 wt.%. In contrast, the absolute mineral abundances of the distant ejecta unit are CPX ~ 14 wt.%, OPX ~ 23 wt.%, Ol ~ 7 wt.% and Pl ~ 56 wt.%. As a comparison, the background absolute mineral abundances are CPX ~ 29 wt.%, OPX ~ 19 wt.%, Ol ~ 13 wt.% and Pl ~ 38 wt.%.

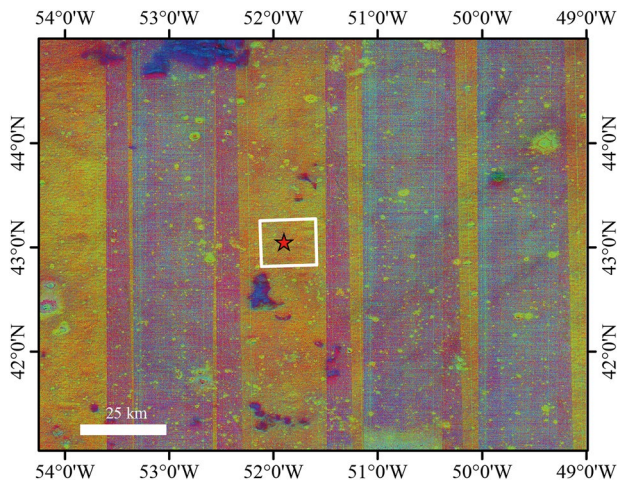


**Figure 5.** The basemap is the RGB composite of ferrous mineral abundance (Lemelin et al., 2015, 2019) covering the CE-5 landing site. The red channel corresponds to CPX, green channel represents OI, and blue channel corresponds to OPX. The red star is the CE-5 landing site. The white square is the area to calculate the average mineral abundance for CE-5 landing site (Table 1).

#### 4.2.2. Copernicus

Copernicus crater is located at 9.64°N and 20.06°W, and has a diameter of 94.30 km. The study area associated with this crater covers a quadrant within 7–12.7°N and 17.3–22.5°W (Figure 6b). The mineral composition of Copernicus ejecta exhibits heterogeneity in the azimuthal direction. The ejecta predominantly extends in a northwest direction (toward the landing site), although a small amount diverges in other directions. The composition of the ejecta appears relatively uniform and is depicted as green in the mineralogical composition map known as the "red spots" (Whitaker, 1972). Shkuratov et al. (2016) suggested that the asymmetry of the ejecta is related to the inclination of the impactor trajectory. Reflecting the analytical approach to the Kepler crater, two ejecta blankets from Copernicus were selected for the study. The absolute mineral abundances of the red spots unit are CPX ~ 6 wt.%, OPX ~ 1 wt.%, OI ~ 7 wt.% and PI ~ 86 wt.%. In contrast, the absolute mineral abundances of the distant ejecta unit are CPX ~ 15 wt.%, OPX ~ 20 wt.%, OI ~ 2 wt.% and PI ~ 63 wt.%.

#### 4.2.3. Sharp B

Sharp B crater is located at 47°N and 45.34°W, northeast of the landing site, and has a diameter of 20.96 km. The study area associated with this crater bounds of 46.6–48°N and 44.1–46.5°W (Figure 6c). The Sharp B crater does

not manifest conspicuous ejecta. Nonetheless, we have selected two distinct areas in the southwest that display differences in composition. The absolute mineral abundances of the area near the crater are CPX ~ 12 wt.%, OPX ~ 17 wt.%, OI ~ 8 wt.% and PI ~ 63 wt.%. Conversely, the absolute mineral abundances of the area farther away from the crater are CPX ~ 11 wt.%, OPX ~ 7 wt.%, OI ~ 17 wt.% and PI ~ 65 wt.%.

#### 4.2.4. Aristarchus

Aristarchus crater is located at 23.74°N and 47.49°W, south of the landing site. It has a diameter of 40.14 km. The study area for Aristarchus encompasses the region within 22.5–25°N and 46.3–49.5°W (Figure 6d). Significant differences in the mineral composition exist between the northern and southern parts of the Aristarchus ejecta. In this study, our study is exclusively directed toward the northern ejecta orientated toward the CE-5 site (indicated by the red square in Figure 6d). We have selected three ejecta blankets and Oceanus Procellarum basalts for analysis. The absolute mineral abundances of the nearby ejecta unit are CPX ~ 28 wt.%, OPX ~ 17 wt.%, OI ~ 11 wt.% and PI ~ 44 wt.%. The unit corresponding to the ejecta at a medium distance from the crater exhibits absolute mineral abundances of CPX ~ 32 wt.%, OPX ~ 17 wt.%, OI ~ 11 wt.% and PI ~ 41 wt.%. Additionally, the distant ejecta unit displayed absolute mineral abundances of CPX ~ 27 wt.%, OPX ~ 19 wt.%, OI ~ 13 wt.% and PI ~ 44 wt.%. For comparative elucidation, the background absolute mineral abundances in the area are CPX ~ 25 wt.%, OPX ~ 17 wt.%, OI ~ 16 wt.% and PI ~ 43 wt.%.

#### 4.2.5. Harpalus

Harpalus crater is located at 52.73°N and 43.49°W, northeast of the landing site, and has a diameter of 39.77 km. The study area for Harpalus is limited to the region encompassed by 7–12.7°N and 17.3–22.5°W. However, the Kaguya mineralogical composite map (Lemelin et al., 2015, 2019) is not available for this region.

### 5. Discussion

#### 5.1. Mineral Composition of the CE-5 Regolith Materials

Upon meticulous examination of the LMS hyperspectral data, we observed that most of the data exhibited high values for B1asy, B1cen, and Area Ratio, which are similar to the spectral features of olivine (Figures 4c and 4e). Nonetheless, the analysis of returned samples from the CE-5 mission indicated very low olivine abundance (He et al., 2022; Jiang et al., 2022; Li et al., 2022; D. Liu et al., 2022; Tian et al., 2021; Zhang et al., 2021). This indicates that the cause of this special spectral feature is not attributable to olivine. The spectral features of Type A CPX are very similar



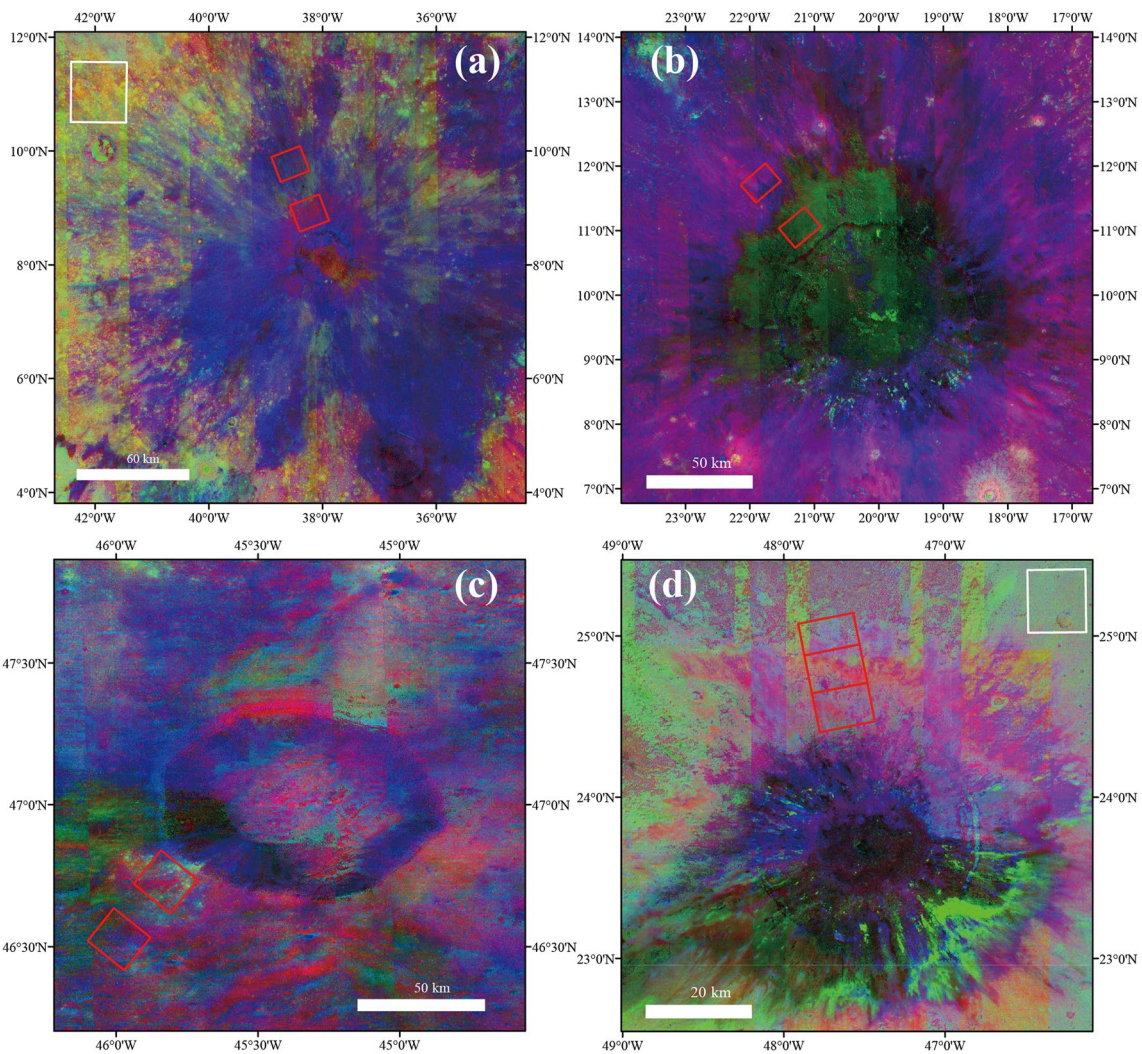


**Figure 6.** The candidate impact craters are considered as potential contributors of a relatively significant number of materials to the CE-5 landing site. These craters include (a) Kepler, (b) Copernicus, (c) Sharp B, and (d) Aristarchus. The basemap is the RGB composite of ferrous mineral abundance (Lemelin et al., 2015, 2019). The red channel corresponds to CPX, green channel represents Ol, and blue channel corresponds to OPX. The red and white squares represent the area to calculate the average mineral abundance for candidate crater ejecta and corresponding background basalt, respectively (Table 1).

to those of olivine, with only a single absorption band at 1  $\mu\text{m}$  and a low Area Ratio, rendering the differentiation between Type A CPX and olivine a challenging endeavor when solely reliant on spectroscopy (Cloutis, 2002).

Moriarty and Pieters (2016) orchestrated a meticulous organization of the pyroxene composition and spectrum in Apollo samples, as cataloged within the Lunar Rock and Mineral Characterization Consortium (LRMCC) and Lunar Soil Characterization Consortium (LSCC). For the LRMCC basalt samples, both high and low calcium pyroxene were observed in all basalt samples (Isaacson, Pieters, et al., 2011; Isaacson, Sarbadhikari, et al., 2011; Klima et al., 2008). The high-calcium pyroxene not only aligns impeccably with the requisites delineated for Type A CPX spectral characterization in Klima et al. (2011) in terms of chemical composition but also conspicuously exhibits Type A CPX spectral characteristics. Similarly, the LSCC soil samples also show the presence of high Wo and Type A CPX spectral characteristics (Pieters, Taylor, McKay, et al., 2000; Taylor et al., 2001, 2010). This suggests that the existence of Type A CPX on the Moon.

Through the analysis of returned samples, we have determined that the high B1asy, B1cen, and low Area Ratio are more plausibly ascribed to the abundant presence of Type A CPX, intermingled with a modest quantity of olivine. Type A CPX is typically characterized by a higher calcium (Ca) content compared to Type B CPX (Adams, 1975), and the pyroxene content within the CE-5 samples is relatively rich in Ca, consistent with the



**Table 1**  
*Averaged Mineral Abundances of the CE-5 Region and Candidate Exotic Material Sources Using the Kaguya Ferrous Mineral Abundance Mosaic (Lemelin et al., 2015, 2019)*

		CPX (wt.%)	OPX (wt.%)	Ol (wt.%)	Pl (wt.%)
Kepler	CE-5	37	9	14	40
	Continuous ejecta	19	24	4	53
	Distant ejecta	14	23	7	56
	Background	29	19	13	38
Copernicus	Red spots <sup>a</sup>	6	1	7	86
	Distant ejecta	15	20	2	63
Sharp B	Nearby unit <sup>b</sup>	12	17	8	63
	Distant unit <sup>b</sup>	11	7	17	65
Aristarchus	Continuous ejecta	28	17	11	44
	Medium ejecta	32	17	11	41
	Distant ejecta	27	19	13	44
	Background	25	17	16	43

*Note.* Validation of the method using spectra of lunar soil of known composition reveals an error in the mineral abundance estimation of  $\pm 8$  wt.% (Lemelin et al., 2015).

<sup>a</sup>Red spots unit is a high albedo unit (Whitaker, 1972) outside the northwest rim of the Copernicus crater. <sup>b</sup>No obvious ejecta blanket of Sharp B crater was observed. We selected units at different distances to analyze different mineral characteristics.

sample results (He et al., 2022; D. Liu et al., 2022). Moreover, the dominant pyroxene mineral in the CE-5 landing region is mainly augite, with an average composition of  $Wo_{32.9}En_{28.2}Fs_{38.9}$  (Li et al., 2022). Klima et al. (2011) obtained spectra of different pyroxene compositions through synthesized pyroxene, and the spectral features of DL-CMP-068 ( $Wo_{30}En_{28}Fs_{42}$ ) were found to be akin to our LMS data (especially D11 in this study), which are essentially similar in composition to the returned samples. Hence, we have determined that the minerals present in the CE-5 materials are primarily composed of two types of clinopyroxene (Type A and B) and plagioclase, as opposed to a significant admixture with olivine.

## 5.2. Mineralogy of the CE-5 Landing Site

Regarding the LMS soil samples, all of them exhibit slight asymmetry in the 1  $\mu$ m band, which is attributed to the significant feldspar content (Cheek & Pieters, 2014). In Figure 4c, all data points lie above the PX-phase and to the left of the Ol-phase. Horgan et al. (2014) categorized such samples as being in the PX-Ol mixing phase. However, their analysis of the band parameter diagrams did not encompass Type A CPX. Considering the presence of Type A CPX, all samples are situated within the mixing phase of Type A CPX and Type B CPX rather than the Ol mixing phase (Figure 4c). This occurrence may be attributed to the influence of partial Ca-rich CPX, which exhibits high B1asy and high B1cen characteristics.

The sample points delineated in Figures 4c–4e sketch a roughly L-shaped domain. We have provided detailed characterization of the previously proposed three groups of soil spectra in Table 2. Most of the soil spectra exhibit moderate-to-high B1cen values ( $>0.95 \mu$ m), moderate-to-high B1asy values ( $>0.15$ ), moderate B2cen values ( $>1.95 \mu$ m), and low Area Ratio values ( $< 1$ ). Group 1 consists of only one member, D12. The characteristics of moderate B1cen and high B2cen in Group 1 are similar to those of the augite phase, but with higher B1asy and lower Area Ratio values. Based on these observations, we propose that Group 1 is predominantly composed of Type A CPX, Type B CPX, and plagioclase. Conversely, Group 2 is characterized by high B1cen values, evoking the diopside phase. However, most members of Group 2 also exhibit moderate B1asy values greater than 0.15, which is a characteristic of Type A CPX, although not as pronounced as in Group 1. Group 2 thus appears to be primarily composed of Type B CPX and plagioclase. In comparison, Group 3 represents a transitional group between the other two groups. It exhibits band center features similar to augite with a slight Type A CPX band feature.

D11 exhibits the same band parameter characteristics as Group 1. Moreover, D11 has an even higher B1asy value compared to the soil spectra. This suggests that the rock situated within the CE-5 landing zone shares a similar composition with the CE-5 lunar soil material. The rock may either represent in situ material that has not undergone weathering into soil or exotic material with a composition akin to that of the landing site.

**Table 2**  
*Classification by Band Parameters of Lunar Mineralogical Spectrometer (LMS) Hyperspectral Spectra*

		B1cen	B1asy	B2cen	Area ratio	CPX type (avg.)	Ca content	Members
Soil	Group 1	moderate (0.97–1 $\mu$ m)	High ( $> 0.35$ )	Moderate	Low	Augite	High	D12
	Group 2	high ( $> 1 \mu$ m)	Moderate (0.15–0.35)	Moderate	Low	Diopside	Moderate	D14, D15
	Group 3	Moderate	Moderate-high	Moderate	Low	Augite	Moderate-high	D8, D9, D10, D16, and D17
Rock		Moderate	High	High	Low	Augite	High	D11

Based on the analysis of LMS spectra, we have suggested that the material composition of the CE-5 landing site is a mixture of two types of clinopyroxene (CPX) and plagioclase (Pl). Furthermore, the composition of CPX within the soil exhibits a lack of uniformity, particularly in the context of calcium (Ca) content.

To compare the laboratory spectra of the returned samples with the LMS spectra. We analyzed the spectra of the returned samples utilizing the spectra provided by D. Liu et al. (2022). D. Liu et al. (2022) procured laboratory spectra of CE5C-S1, CE5C-S2, and CE5C-S3 (CE5C0800YJFM001-1, CE5C0100YJFM002-1, and CE5C0100YJFM002-2). We used this spectrum (450–2,500 nm) to recalculate the band parameters. The recalculated band parameters for the laboratory spectra are elucidated in Table S1 in Supporting Information S1. The results show that the band parameters (B1cen, B1asy, B2cen, and Area Ratio) obtained from the three laboratory spectra are exceedingly analogous. The mean B1cen value is 1.02  $\mu\text{m}$ . The mean B1asy is 0.26. The mean B2cen is 2.19  $\mu\text{m}$ . The mean Area Ratio is 0.50. Barring B2cen, the characterization of the other parameters (B1cen, B1asy, and area ratio) is similar to Group 2 of LMS spectra, showing high B1cen ( $> 1 \mu\text{m}$ ), moderate B1asy (0.15–0.35), and low Area Ratio ( $< 1$ ). This is the spectral characterization of Type A CPX. B2cen surpassed the value of all LMS spectra. However, since the B2cen of Type B CPX ranges from 2.1 to 2.35, we considered that both the B2cen of the laboratory and LMS spectra exhibit the characteristics of Type B CPX. In summary, we considered that the laboratory spectra are similar to the LMS spectra in that they are dominated by the two kinds of CPX.

### 5.3. Mineralogy of Candidate Source Craters

The dominance of clinopyroxene (CPX) and plagioclase (Pl) as the main components of the exotic material at the CE-5 landing site may be attributed to the mineral composition of the site itself. Consequently, it is crucial to determine the relative content of CPX, orthopyroxene (OPX), and olivine (Ol) in the candidate source craters (Kepler, Copernicus, Sharp B, Aristarchus, and Harpalus).

Owing to the spectral similarities between Type A CPX and olivine, we suggest that a significant amount of Type A CPX may have been misidentified as olivine in previous studies based on the MI-derived ferrous mineral weight percentage (Qian, Xiao, Wang, et al., 2021). This misidentification has engendered the erroneous identification of CPX-enriched zones as olivine-enriched areas based on remote sensing data, such as in the CE-5 region. The mineral content derived from the MI also concurs with these previous findings. Although the MI-derived mineral content measurements may not reflect the precise ground truth compositions, they remain instrumental for comparing the content of optical minerals. Considering that OPX was rarely found in the returned samples from CE-5 (He et al., 2022; Li et al., 2021, 2022), the craters dominated by OPX and corresponding to the ejecta material are unlikely to have made a significant contribution to the exotic material in the CE-5 region. In this discussion, we analyze the content of CPX + Ol as a combined parameter, alongside the individual mineral contents of OPX and Pl, considering the mixing of Type A CPX in both parameters.

Both the distal and near northwestern ejecta units of Kepler crater (denoted as red and blue unit in Figure 6a) exhibit lower content of CPX and Ol, and higher content of OPX and Pl compared to the Oceanus Procellarum basalt unit. The CPX + Ol content is about 20 wt.% lower than the background, whilst the OPX content is about 5 wt.% higher, and the Pl content is approximately 5 wt.% lower than the background. These findings signify that the mineral composition of the northwestern crater ejecta is primarily composed of Pl and OPX. This composition differs markedly from the anticipated composition of the exotic material that is conjectured to contribute significantly to the CE-5 landing site. Consequently, the Kepler crater is not regarded as the source of the CE-5 exotic material.

The red spots observed in the Copernicus crater are unique in nature. The red spot unit (illustrated as the green unit in Figure 6b) is believed to have formed through extrusion and is unlikely to have been ejected far away from the crater (Shkuratov et al., 2016). According to Pieters et al. (1985), the uppermost strata of a deposit in locales with continuous ejecta are not as influenced by basal substrate mixing. In our investigation, we explored whether the distant ejecta unit (depicted as the purple unit in Figure 6b) could serve as a possible source for the exotic CE-5 material. The Copernicus ejecta is widely distributed around the crater. The absolute mineral abundances of the distant ejecta unit are CPX + Ol  $\sim 17$  wt.%, OPX  $\sim 20$  wt.% and Pl  $\sim 63$  wt.%. This indicates that the distant ejecta unit is characterized by a high plagioclase content along with some other ferrous minerals. However, the compositions of both the CPX + Ol and OPX contents are similar, whereas there is no significant manifestation

of OPX in the CE-5 landing region. Hence, we propose that the Copernicus crater is not the source of the exotic materials discovered at the CE-5 landing site.

Sharp B crater, located in the highlands, lacks obvious ejecta blankets. The units present in the southwest region outside the crater rim do not exhibit significant differences in composition compared with the surrounding highlands. The unit represented by the green spot was found near the southwest side of the crater, close to the rim (Figure 6c). These spots could potentially be olivine-enriched melts. However, upon examination, we found that the composition of the Sharp B crater ejecta is similar to that of the highlands, primarily composed of plagioclase (Pl). Therefore, the Sharp B crater is not considered a major source of the exotic material found at the CE-5 landing site.

The mineral abundance features of the Aristarchus crater ejecta on the northwest side exhibit a metamorphosis with an escalating radial distance from the center. We have selected three sub-units within the northwest ejecta unit that exhibit different characteristics based on their distance from the crater center. The near ejecta unit shows characteristics similar to the distant ejecta unit. Both units exhibited lower Ol content ( $\sim 11$  wt.%) in comparison to the Oceanus Procellarum basalts ( $\sim 13$  wt.%). The ejecta unit located between the far and near units shows a higher CPX content compared to the other ejecta units. Nonetheless, the disparities in mineralogical contents among these three ejecta units and the backdrop are marginal, less than 2 wt.%. This suggests that these three ejecta units are similar in composition to the background components. The overall composition of the three ejecta units is characterized by a high content of CPX + Ol and low content of OPX, as derived from the mineral abundance data obtained from the MI. However, owing to the presence of Type A CPX being mistakenly identified as Ol, we cannot determine the exact composition of the Aristarchus crater northwest ejecta based solely on the mineral abundance data. However, owing to the misidentification of Type A CPX as olivine, the precise composition of the northwest ejecta from Aristarchus crater remains elusive when solely reliant upon the mineral abundance data.

#### 5.4. Analysis of Potential Source Craters

Owing to the constraints of the ferrous mineral abundance mosaic in fully capturing all the optical features of potential craters, further analysis of specific craters is necessary. Considering the composition of the lunar soil in the CE-5 landing region, the exotic ejecta that significantly contribute to the landing region are expected to be rich in CPX (either Type A or B), while being poor in OPX and Ol. The spectral information of the Aristarchus ejecta also exhibits mineralogical characteristics akin to those observed at the CE-5 landing site, suggesting that it could have made a significant contribution to the material comprising the landing region. In contrast, the Kaguya mineralogical composite map is not available for the Harpalus crater region. Hence, we consider both the Aristarchus and Harpalus craters as potential impact craters meriting further analysis. The M3 spectral data covers both the two craters and will be utilized for additional investigations into their mineral composition.

The M3 data were collected from the northern ejecta of the Aristarchus crater, extending from the rim toward the landing site (Figure 7a). Table S2 in Supporting Information S1 presents the band parameters for the continuum-removed spectra. No notable compositional variations are discerned across the examined points. The B1cen values are approximately  $0.99 \mu\text{m}$ , whilst the B2cen values are above  $2.0 \mu\text{m}$ . All  $1 \mu\text{m}$  absorption bands exhibit symmetrical shapes, and the B1asy values are low. These results indicate that the spectral features of the Aristarchus northern ejecta are predominantly characterized by Type B CPX, with some OPX mixing. The mineral composition of this ejecta unit is primarily composed of Type B CPX, Pl, with a small amount of OPX.

The Kaguya mineralogical composite map for Harpalus crater is not available; therefore, we solely used M3 data in the analysis. The M3 data for Harpalus was collected as a series of points extending from the crater rim toward the landing site in a southwest direction (Figure 8). Table S3 in Supporting Information S1 presents the band parameters for the continuum removed spectra. HA-1 to HA-6 correspond to the continuous ejecta along the southwest direction of Harpalus. The majority of the B1cen values are below  $0.9 \mu\text{m}$ , except for HA-3, which is higher than  $1 \mu\text{m}$ . The B1asy values in this area are predominantly lower than 0 or slightly higher than 0, indicating the dominance of pyroxene (PX). Conversely, HA-7 to HA-13 represent the southwest discontinuous ejecta of Harpalus crater. In this instance, the B1cen values are higher than those of the continuous ejecta, ranging from  $0.97$  to  $1.3 \mu\text{m}$ . The B2cen values range from  $1.91$  to  $2.0 \mu\text{m}$ , whilst the B1asy values are mostly higher than 0.08 with a maximum value of 0.15. These spectral band parameters suggest that the spectral features of the southwest discontinuous ejecta of Harpalus are predominantly influenced by Type B clinopyroxene (CPX) and plagioclase (Pl), with some orthopyroxene (OPX) mixing. The mineral compo-



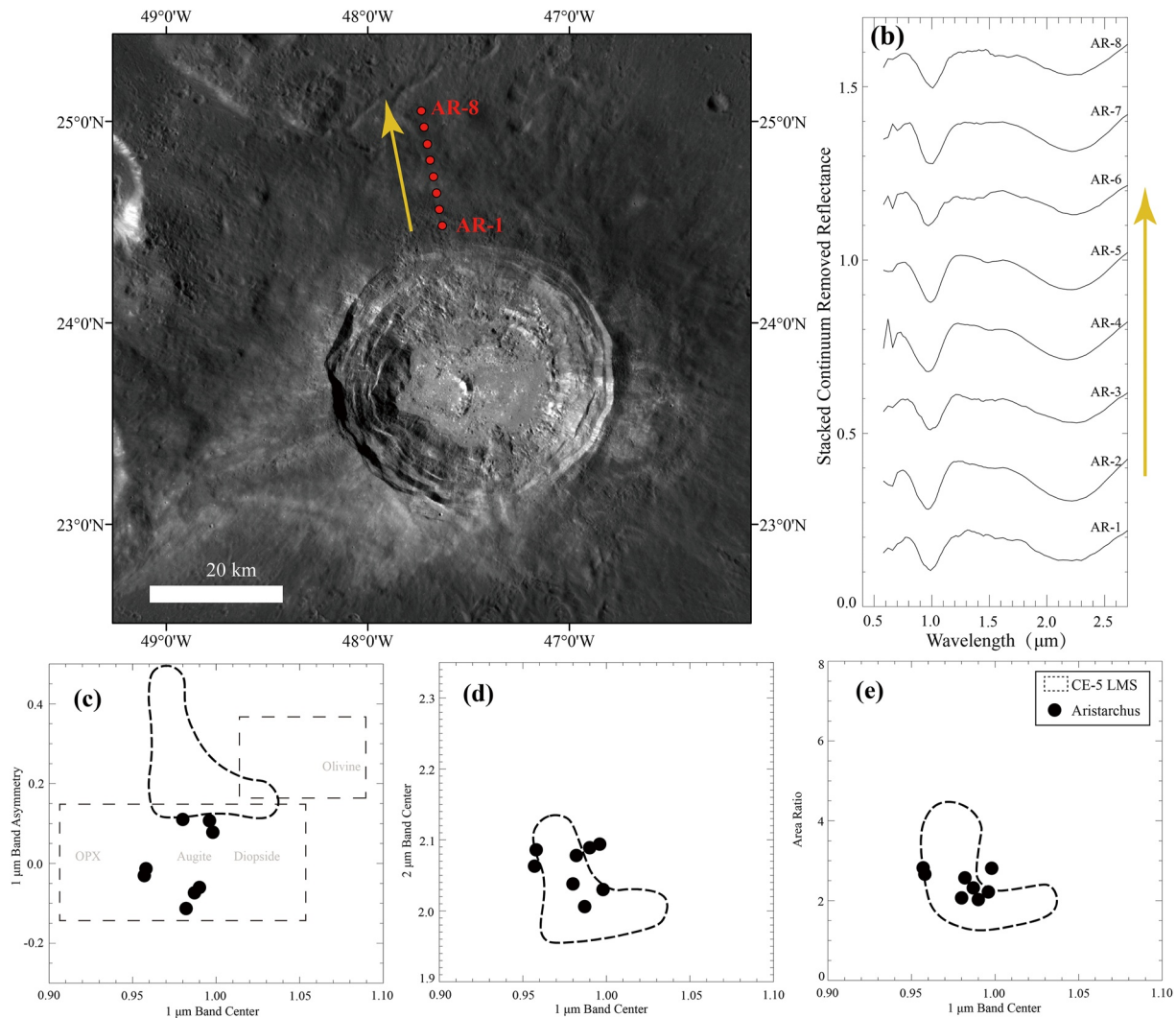


**Figure 7.** (a) Aristarchus crater, with the basemap is from LROC WAC global mosaic (NASA/ASU). (b) Continuum-removed spectra obtained from M3 observation M3G20090418T132620. The eight spectra were obtained from the north ejecta, at a distance equal to the rim of the Aristarchus crater, extending toward the CE-5 landing site. The positions shown in (a) correspond to the direction of the yellow arrow. (c–e) Comparison of the 1 and 2  $\mu\text{m}$  band parameters between the spectra from the Aristarchus ejecta (black points) and the CE-5 landing site. The region enclosed by the dashed line indicates the range of the CE-5 LMS data, like Figures 4c–4e. For additional details regarding the samples, please refer to Tables S1 and S2 in Supporting Information S1.

sition of this ejecta unit is primarily composed of Type B CPX, Pl, with a modicum of OPX. The continuous and discontinuous ejecta exhibit different spectral characteristics, but both spectra are dominated by PX. Both OPX and CPX are present in the pyroxene mixture. Whilst the discontinuous ejecta may be mixed with bedrock material, we propose that the composition of the southwest ejecta of Harpalus is primarily CPX and Pl, with some OPX.

In terms of the related ejecta from the five investigated craters, the Kepler crater is characterized by a higher abundance of OPX and Pl. Copernicus and Sharp B craters exhibit higher abundance of Pl. Conversely, Aristarchus and Harpalus craters are characterized by a higher abundance of CPX and Pl, with a smaller amount of OPX. Consequently, it is plausible that Aristarchus and Harpalus craters have contributed a greater quantity of exotic materials to the CE-5 landing site compared to other distant impact craters. Moreover, the abundance of OPX in the ejecta of Aristarchus and Harpalus does not plummet to the low levels observed at the CE-5 site, suggesting that the presence of exotic materials at the CE-5 landing site is minimal.

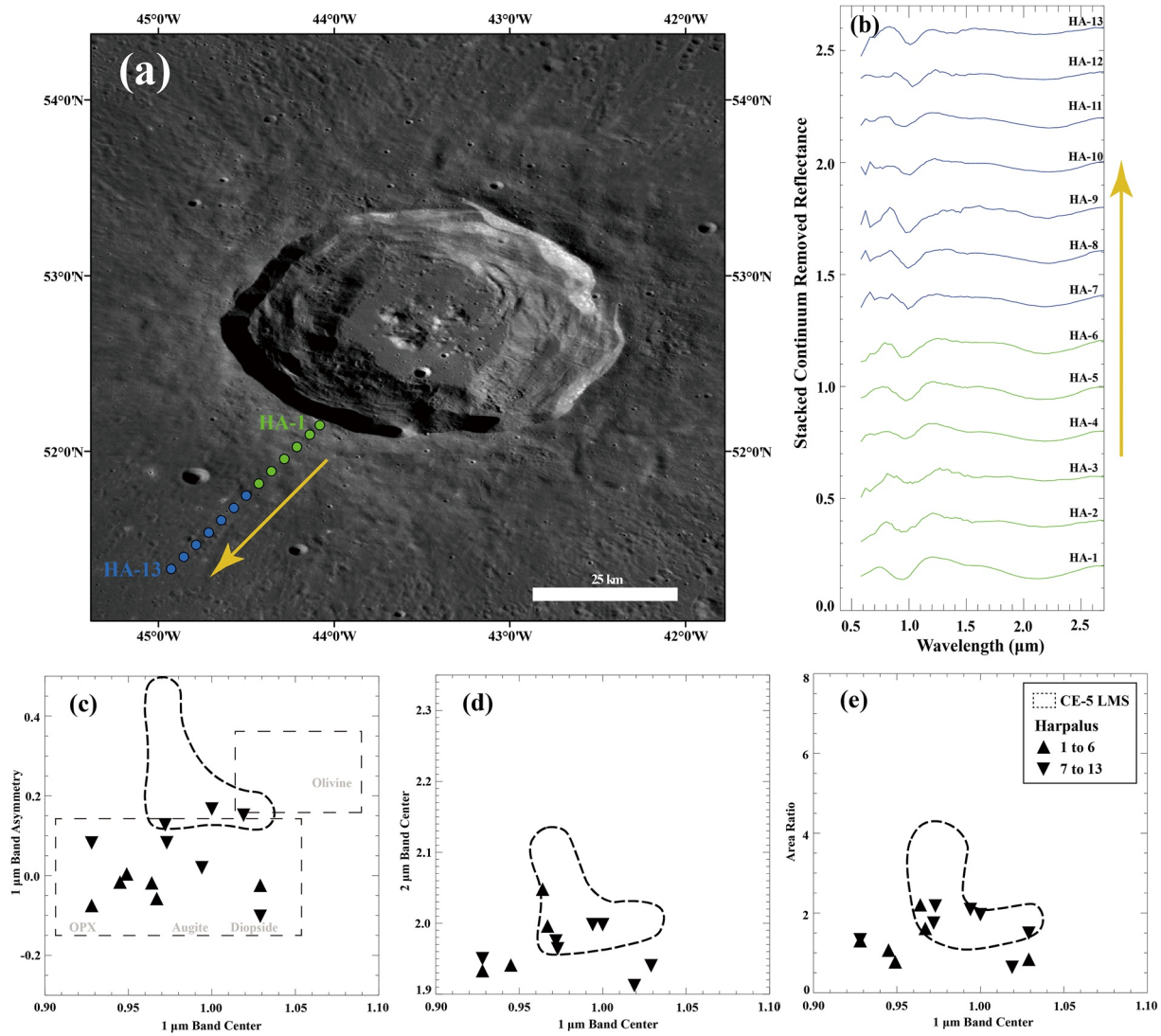


**Figure 8.** (a) Harpalus crater. The basemap is from the LROC WAC global mosaic (NASA/ASU). The green and blue points represent the continuous and discontinuous ejecta, respectively. (b) Continuum-removed spectra obtained from M3 observation M3G20090209T033051. The 13 spectra were collected within the northern ejecta, at a distance equal to the distance from the rim of the Harpalus crater to the CE-5 landing site. The positions shown in (a) and the spectra in (b) correspond to the direction of the yellow arrow. (c–e) Comparison of the 1 and 2  $\mu\text{m}$  band parameters between the spectra from the Harpalus ejecta and the CE-5 landing site. The black upward-pointing triangles indicate the Harpalus continuous ejecta, while the black inverted triangles indicate the Harpalus discontinuous ejecta. The range outlined by the dashed line mirrors the LMS data range, as in Figures 4c–4e. For additional details regarding the samples, please refer to Tables S1 and S3 in Supporting Information S1.

## 6. Conclusions

In this study, we examined the spectra obtained by the LMS instrument from the area surrounding the CE-5 lander, in conjunction with MI and M3 data from distant ejecta source craters. By analyzing the in situ CE-5 spectra as ground truth and comparing them with the results of returned samples, we determined that the samples collected at the landing site consist predominantly of a mixture of two types of CPX and Pl. We also found that the composition of CPX in the soil was not consistent throughout the region. The similarity in spectral characteristics between CPX type A and Ol highlights the need for corrections in olivine-rich mare regions based on remote sensing data. Moreover, our analysis suggests that exotic materials constitute a relatively small proportion of the composition at the CE-5 landing site. The main sources of these exotics are Harpalus and Aristarchus craters, both of which are characterized by a high abundance of Type B CPX and Pl.

## Data Availability Statement

The LMS spectra used in this article can be accessed from Yang (2023). The CE-1 DOM global mosaic is provided by China National Space Agency and the Science and Application Center for Moon and Deep Space Exploration, and accessible from <https://moon.bao.ac.cn/ce5web/moonGisMap.do> with a register account. LROC WAC Global Morphology Mosaic is accessible from [https://astrogeology.usgs.gov/search/map/Moon/LRO/LROC\\_WAC/Lunar\\_LRO\\_LROC-WAC\\_Mosaic\\_global\\_100m\\_June2013](https://astrogeology.usgs.gov/search/map/Moon/LRO/LROC_WAC/Lunar_LRO_LROC-WAC_Mosaic_global_100m_June2013). KAGUYA Multiband Imager mineral maps are accessible from [https://planetarymaps.usgs.gov/mosaic/Lunar\\_MI\\_mineral\\_maps/](https://planetarymaps.usgs.gov/mosaic/Lunar_MI_mineral_maps/). Moon Mineralogy Mapper data are accessible from <https://pds-imaging.jpl.nasa.gov/volumes/m3.html> refer from Erick Malaret (2011).

## Acknowledgments

The Chang'E-5 LMS data used in this work is processed and produced by "Ground Research and Application System" (GRAS) of China's Lunar and Planetary Exploration Program. We used Goody-1 high performance cluster of the School of Earth Science at the China University of Geosciences to process data in this study. The authors extend our appreciation to Rui Xu, Chunlai Li, and Zhiping He of the Key Laboratory of Space Active Opto-Electronics Technology, Shanghai Institute of Technical Physics for discussing with us spectral data processing and the efforts of the science teams involved in the production of all the data sets used, particularly the LROC, MI, and M3. The authors thank editor Prof. Dr. Deanne Rogers, and two anonymous reviewers for their constructive comments. Dr. Xing Wu provided the image acquired by the LMS multispectral mode. This study was funded by M-0016 Sino-German mobility project granted by Sino-German Science Center of the National Natural Science Foundation of China, Shanghai Sailing Program (22YF1447300) and the Outstanding Youth Team Project of China University of Geosciences, Wuhan (G1323523042).

## References

- Adams, J. B. (1975). Interpretation of visible and near-infrared diffuse reflectance spectra of pyroxenes and other rock-forming minerals. *Infrared and Raman Spectroscopy of Lunar and Terrestrial Minerals*, 91–116. <https://doi.org/10.1016/b978-0-12-399950-4.50009-4>
- Adams, J. B., & Goullaud, L. (1978). Plagioclase feldspars-visible and near infrared diffuse reflectance spectra as applied to remote sensing. In *Paper presented at the lunar and planetary science conference proceedings*.
- Besse, S., Boardman, J., Nettles, J., Staid, M., Sunshine, J., Li, J.-Y., et al. (2011). Deriving a photometric model for the Moon Mineralogy Mapper data (M3). In *Paper presented at the 42nd annual lunar and planetary science conference*.
- Boardman, J. W., Pieters, C. M., Green, R. O., Lundeen, S. R., Varanasi, P., Nettles, J., et al. (2011). Measuring moonlight: An overview of the spatial properties, lunar coverage, selenolocation, and related Level 1B products of the Moon Mineralogy Mapper. *Journal of Geophysical Research*, 116, E00G14. <Go to ISI>://WOS:000291318700001. <https://doi.org/10.1029/2010je003730>
- Che, X., Nemchin, A., Liu, D., Long, T., Wang, C., Norman, M. D., et al. (2021). Age and composition of young basalts on the Moon, measured from samples returned by Chang'E-5. *Science*, 374(6569), 887–890. <Go to ISI>://WOS:000717915400038. <https://doi.org/10.1126/science.abl7957>
- Cheek, L. C., & Pieters, C. M. (2014). Reflectance spectroscopy of plagioclase-dominated mineral mixtures: Implications for characterizing lunar anorthosites remotely. *American Mineralogist*, 99(10), 1871–1892. <Go to ISI>://WOS:000342956700008. <https://doi.org/10.2138/am-2014-4785>
- Clark, R. N., Pieters, C. M., Green, R. O., Boardman, J. W., & Petro, N. E. (2011). Thermal removal from near-infrared imaging spectroscopy data of the Moon. *Journal of Geophysical Research*, 116, E00G16. <Go to ISI>://WOS:000292114100001. <https://doi.org/10.1029/2010je003751>
- Cloutis, E. A. (2002). Pyroxene reflectance spectra: Minor absorption bands and effects of elemental substitutions. *Journal of Geophysical Research*, 107(E6), 5039. <Go to ISI>://WOS:000178977900008. <https://doi.org/10.1029/2001je001590>
- Cloutis, E. A., & Gaffey, M. J. (1991). Spectral-compositional variations in the constituent minerals of mafic and ultramafic assemblages and remote sensing implications. *Earth, Moon, and Planets*, 53(1), 11–53. <Go to ISI>://WOS:A1991FX86100002. <https://doi.org/10.1007/bf00116217>
- Collins, G. S., Melosh, H. J., & Osinski, G. R. (2012). The impact-cratering process. *Elements*, 8(1), 25–30. <Go to ISI>://WOS:000301080600006. <https://doi.org/10.2113/gselements.8.1.25>
- Green, R. O., Pieters, C., Mouroulis, P., Eastwood, M., Boardman, J., Glavich, T., et al. (2011). The Moon mineralogy mapper (M3) imaging spectrometer for lunar science: Instrument description, calibration, on-orbit measurements, science data calibration and on-orbit validation. *Journal of Geophysical Research*, 116, E00G19. <https://doi.org/10.1029/2011je003797>
- Gueymard, C. A. (2004). The Sun's total and spectral irradiance for solar energy applications and solar radiation models. *Solar Energy*, 76(4), 423–453. <Go to ISI>://WOS:000220241000007. <https://doi.org/10.1016/j.solener.2003.08.039>
- Hapke, B. (2012). *Theory of reflectance and emittance spectroscopy*. Cambridge university press.
- He, Q., Li, Y., Baziotis, I., Qian, Y., Xiao, L., Wang, Z., et al. (2022). Detailed petrogenesis of the unsampled Oceanus procellarum: The case of the Chang'E-5 mare basalts. *Icarus*, 383, 115082. <https://doi.org/10.1016/j.icarus.2022.115082>
- Hicks, M. D., Buratti, B. J., Nettles, J., Staid, M., Sunshine, J., Pieters, C. M., et al. (2011). A photometric function for analysis of lunar images in the visual and infrared based on Moon Mineralogy Mapper observations. *Journal of Geophysical Research*, 116, E00G15. <Go to ISI>://WOS:000291825400001. <https://doi.org/10.1029/2010je003733>
- Hiesinger, H., Head, J. W., Wolf, U., Jaumann, R., & Neukum, G. (2003). Ages and stratigraphy of mare basalts in Oceanus procellarum, mare Nubium, mare Cognitum, and mare Insularum. *Journal of Geophysical Research*, 108(E7). <Go to ISI>://WOS:000184004700001. <https://doi.org/10.1029/2002je001985>
- Horgan, B. H. N., Cloutis, E. A., Mann, P., & Bell, J. F. (2014). Near-infrared spectra of ferrous mineral mixtures and methods for their identification in planetary surface spectra. *Icarus*, 234, 132–154. <Go to ISI>://WOS:000334560500011. <https://doi.org/10.1016/j.icarus.2014.02.031>
- Hou, X., Fu, X., Qiao, L., Li, B., Yin, C., Zhang, J., & Ling, Z. (2022). Absolute model ages of three craters in the vicinity of the Chang'E-5 landing site and their geologic implications. *Icarus*, 372, 114730. <https://doi.org/10.1016/j.icarus.2021.114730>
- Huang, J., Xie, J., Huang, C., Lin, H., Zhong, J., He, Q., et al. (2020). Diverse rock types detected in the lunar South Pole–Aitken Basin by the Chang'E-4 lunar mission. *Geology*, 48(7), 723–727. <https://doi.org/10.1130/g47280.1>
- Isaacson, P. J., Pieters, C., Hiroi, T., Liu, Y., Dhingra, D., Klima, R., & Taylor, L. (2011). Reflectance spectroscopy of ilmenite: New constraints from Apollo sample measurements. In *Paper presented at the 42nd annual lunar and planetary science conference*.
- Isaacson, P. J., Petro, N. E., Pieters, C. M., Besse, S., Boardman, J. W., Clark, R. N., et al. (2013). Development, importance, and effect of a ground truth correction for the Moon Mineralogy Mapper reflectance data set. *Journal of Geophysical Research: Planets*, 118(3), 369–381. <Go to ISI>://WOS:000318243300001. <https://doi.org/10.1002/jgre.20048>
- Isaacson, P. J., Sarbadhikari, A. B., Pieters, C. M., Klima, R. L., Hiroi, T., Liu, Y., & Taylor, L. A. (2011). The lunar rock and mineral characterization consortium: Deconstruction and integrated mineralogical, petrologic, and spectroscopic analyses of mare basalts. *Meteoritics & Planetary Sciences*, 46(2), 228–251. <https://doi.org/10.1111/j.1945-5100.2010.01148.x>
- Jia, B., Fa, W., Xie, M., Tai, Y., & Liu, X. (2021). Regolith properties in the Chang'E-5 landing region of the Moon: Results from multi-source remote sensing observations. *Journal of Geophysical Research: Planets*, 126(7), e2021JE006934. <Go to ISI>://WOS:000679848100007. <https://doi.org/10.1029/2021je006934>



- Jiang, Y., Li, Y., Liao, S., Yin, Z., & Hsu, W. (2022). Mineral chemistry and 3D tomography of a Chang'E 5 high-Ti basalt: Implication for the lunar thermal evolution history. *Science Bulletin*, 67(7), 755–761. <https://doi.org/10.1016/j.scib.2021.12.006>
- King, T. V. V., & Ridley, W. I. (1987). Relation of the spectroscopic reflectance of olivine to mineral chemistry and some remote sensing implications. *Journal of Geophysical Research*, 92(B11), 11457–11469. <https://doi.org/10.1029/jb092ib11p11457>
- Klima, R. L., Dyar, M. D., & Pieters, C. M. (2011). Near-infrared spectra of clinopyroxenes: Effects of calcium content and crystal structure. *Meteoritics & Planetary Sciences*, 46(3), 379–395. <Go to ISI>://WOS:000288500900003. <https://doi.org/10.1111/j.1945-5100.2010.01158.x>
- Klima, R. L., Pieters, C. M., & Dyar, M. D. (2008). Characterization of the 1.2  $\mu\text{m}$  M1 pyroxene band: Extracting cooling history from near-IR spectra of pyroxenes and pyroxene-dominated rocks. *Meteoritics & Planetary Sciences*, 43(10), 1591–1604. <https://doi.org/10.1111/j.1945-5100.2008.tb00631.x>
- Kodama, S., Ohtake, M., Yokota, Y., Iwasaki, A., Haruyama, J., Matsunaga, T., et al. (2010). Characterization of multiband imager aboard SELENE. *Space Science Reviews*, 154(1–4), 79–102. <Go to ISI>://WOS:000284578500005. <https://doi.org/10.1007/s11214-010-9661-z>
- Lemelin, M., Lucey, P. G., Miljković, K., Gaddis, L. R., Hare, T., & Ohtake, M. (2019). The compositions of the lunar crust and upper mantle: Spectral analysis of the inner rings of lunar impact basins. *Planetary and Space Science*, 165, 230–243. <Go to ISI>://WOS:000468702500020. <https://doi.org/10.1016/j.pss.2018.10.003>
- Lemelin, M., Lucey, P. G., Song, E., & Taylor, G. J. (2015). Lunar central peak mineralogy and iron content using the Kaguya Multiband Imager: Reassessment of the compositional structure of the lunar crust. *Journal of Geophysical Research: Planets*, 120(5), 869–887. <Go to ISI>://WOS:000356434600003. <https://doi.org/10.1002/2014je004778>
- Li, C., Hu, H., Yang, M.-F., Pei, Z.-Y., Zhou, Q., Ren, X., et al. (2022). Characteristics of the lunar samples returned by the Chang'E-5 mission. *National Science Review*, 9(2). <Go to ISI>://WOS:000753113800002. <https://doi.org/10.1093/nsr/nwab188>
- Li, Q.-L., Zhou, Q., Liu, Y., Xiao, Z., Lin, Y., Li, J.-H., et al. (2021). Two-billion-year-old volcanism on the Moon from Chang'E-5 basalts. *Nature*, 600(7887), 54–58. <Go to ISI>://WOS:000722542800002. <https://doi.org/10.1038/s41586-021-04100-2>
- Lin, H., Li, S., Lin, Y., Liu, Y., Wei, Y., Yang, W., et al. (2021). Thermal modeling of the lunar regolith at the Chang'E-4 landing site. *Geophysical Research Letters*, 48(6), e2020GL091687. <Go to ISI>://WOS:000635209100007. <https://doi.org/10.1029/2020gl091687>
- Liu, D., Wang, X., Liu, J., Liu, B., Ren, X., Chen, Y., et al. (2022). Spectral interpretation of late-stage mare basalt mineralogy unveiled by Chang'E-5 samples. *Nature Communications*, 13(1), 5965. <Go to ISI>://WOS:000867457000017. <https://doi.org/10.1038/s41467-022-33670-6>
- Liu, J. J., Liu, B., Ren, X., Li, C. L., Shu, R., Guo, L., et al. (2022). Evidence of water on the lunar surface from Chang'E-5 in-situ spectra and returned samples. *Nature Communications*, 13(1), 3119. <Go to ISI>://WOS:000811535600027. <https://doi.org/10.1038/s41467-022-30807-5>
- Lucey, P. G., Blewett, D. T., Taylor, G. J., & Hawke, B. R. (2000). Imaging of lunar surface maturity. *Journal of Geophysical Research*, 105(E8), 20377–20386. <Go to ISI>://WOS:000089003600015. <https://doi.org/10.1029/1999je001110>
- Lucey, P. G., Norman, J. A., Crites, S. T., Taylor, G. J., Hawke, B. R., Lemelin, M., & Melosh, H. J. (2014). A large spectral survey of small lunar craters: Implications for the composition of the lunar mantle. *American Mineralogist*, 99(11–12), 2251–2257. <Go to ISI>://WOS:000345058200012. <https://doi.org/10.2138/am-2014-4854>
- Lv, G., Li, J., Li, C., Jin, J., Lin, Y., Xu, R., & He, Z. (2022). Temperature correction and result evaluation of lunar mineralogical spectrometer for Chang'E-5 mission. *IEEE Transactions on Geoscience and Remote Sensing*, 60, 1–8. <https://doi.org/10.1109/tgrs.2021.3112743>
- Malaret, E. (2011). CH1-ORB Moon M3 4 L2 reflectance near-IR spectral IMGS V1.0 [Dataset]. NASA Planetary Data System. <https://doi.org/10.17189/1520414>
- Melosh, H. J. (1989). *Impact cratering: A geologic process*. Oxford University Press. Clarendon Press.
- Moriarty, D. P., & Pieters, C. M. (2016). Complexities in pyroxene compositions derived from absorption band centers: Examples from Apollo samples, HED meteorites, synthetic pure pyroxenes, and remote sensing data. *Meteoritics & Planetary Sciences*, 51(2), 207–234. <Go to ISI>://WOS:000370156000001. <https://doi.org/10.1111/maps.12588>
- Ohtake, M., Haruyama, J., Matsunaga, T., Yokota, Y., Morota, T., & Honda, C. (2008). Performance and scientific objectives of the SELENE (KAGUYA) multiband imager. *Earth Planets and Space*, 60(4), 257–264. <Go to ISI>://WOS:000256150200003. <https://doi.org/10.1186/bf03352789>
- Papike, J., Taylor, L., & Simon, S. (1991). Lunar minerals. Lunar sourcebook: A user's guide to the Moon (pp. 121–181).
- Pieters, C. M., Taylor, L., McKay, D., Wentworth, S., Morris, R., & Keller, L. (2000). Spectral characterization of lunar mare soils. In *Paper presented at the lunar and planetary science conference*.
- Pieters, C. M., Adams, J. B., Mouginiis-Mark, P. J., Zisk, S. H., Smith, M. O., Head, J. W., & McCord, T. B. (1985). The nature of crater rays: The Copernicus example. *Journal of Geophysical Research*, 90(B14), 12393–12413. <https://doi.org/10.1029/jb090ib14p12393>
- Pieters, C. M., Taylor, L. A., Noble, S. K., Keller, L. P., Hapke, B., Morris, R. V., et al. (2000). Space weathering on airless bodies: Resolving a mystery with lunar samples. *Meteoritics & Planetary Sciences*, 35(5), 1101–1107. <Go to ISI>://WOS:000089736400022. <https://doi.org/10.1111/j.1945-5100.2000.tb01496.x>
- Pieters, Boardman, J., Buratti, B., Chatterjee, A., Clark, R., Glavich, T., et al. (2009). The Moon mineralogy mapper (M<sup>3</sup>) on chandrayaan-1. *Current Science*, 500–505.
- Qian, Y., Xiao, L., Head, J. W., van der Bogert, C. H., Hiesinger, H., & Wilson, L. (2021). Young lunar mare basalts in the Chang'e-5 sample return region, northern Oceanus Procellarum. *Earth and Planetary Science Letters*, 555, 116702. <Go to ISI>://WOS:000604582900004. <https://doi.org/10.1016/j.epsl.2020.116702>
- Qian, Y., Xiao, L., Wang, Q., Head, J. W., Yang, R., Kang, Y., et al. (2021). China's Chang'E-5 landing site: Geology, stratigraphy, and provenance of materials. *Earth and Planetary Science Letters*, 561, 116855. <Go to ISI>://WOS:000631258000017. <https://doi.org/10.1016/j.epsl.2021.116855>
- Qian, Y. Q., Xiao, L., Zhao, S. Y., Zhao, J. N., Huang, J., Flahaut, J., et al. (2018). Geology and scientific significance of the Rümker region in northern Oceanus Procellarum: China's Chang'E-5 landing region. *Journal of Geophysical Research: Planets*, 123(6), 1407–1430. <https://doi.org/10.1029/2018je005595>
- Schade, U., Wasch, R., & Moroz, L. (2004). Near-infrared reflectance spectroscopy of Ca-rich clinopyroxenes and prospects for remote spectral characterization of planetary surfaces. *Icarus*, 168(1), 80–92. <Go to ISI>://WOS:000220161400008. <https://doi.org/10.1016/j.icarus.2003.10.016>
- Shkuratov, Y., Kaydash, V., Rohacheva, L., Korokhin, V., Ivanov, M., Velikodsky, Y., & Videen, G. (2016). Comparison of lunar red spots including the crater Copernicus. *Icarus*, 272, 125–139. <https://doi.org/10.1016/j.icarus.2016.02.034>
- Sunshine, J. M., & Pieters, C. M. (1998). Determining the composition of olivine from reflectance spectroscopy. *Journal of Geophysical Research*, 103(E6), 13675–13688. <Go to ISI>://WOS:000076969700005. <https://doi.org/10.1029/98je01217>
- Taylor, L. A., Pieters, C., Patchen, A., Taylor, D.-H. S., Morris, R. V., Keller, L. P., & McKay, D. S. (2010). Mineralogical and chemical characterization of lunar highland soils: Insights into the space weathering of soils on airless bodies. *Journal of Geophysical Research*, 115(E2), E02002. <https://doi.org/10.1029/2009je003427>

- Taylor, L. A., Pieters, C. M., Keller, L. P., Morris, R. V., & McKay, D. S. (2001). Lunar Mare Soils: Space weathering and the major effects of surface-correlated nanophase Fe. *Journal of Geophysical Research*, *106*(E11), 27985–27999. <https://doi.org/10.1029/2000je001402>
- Tian, H.-C., Wang, H., Chen, Y., Yang, W., Zhou, Q., Zhang, C., et al. (2021). Non-KREEP origin for Chang'e-5 basalts in the Procellarum KREEP terrane. *Nature*, *600*(7887), 59–63. <Go to ISI>://WOS:000722542800003. <https://doi.org/10.1038/s41586-021-04119-5>
- Wang, J., Zhang, Y., Di, K., Chen, M., Duan, J., Kong, J., et al. (2021). Localization of the Chang'E-5 lander using radio-tracking and image-based methods. *Remote Sensing*, *13*(4), 590. <Go to ISI>://WOS:000624412600001. <https://doi.org/10.3390/rs13040590>
- Warren, B., & Lawrence Bragg, W. (1929). XII. The structure of diopside, CaMg (SiO<sub>3</sub>)<sub>2</sub>. *Zeitschrift für Kristallographie - Crystalline Materials*, *69*(1–6), 168–193. <https://doi.org/10.1524/zkri.1929.69.1.168>
- Whitaker, E. A. (1972). Lunar color boundaries and their relationship to topographic features: A preliminary survey. *The Moon*, *4*(3–4), 348–355. <https://doi.org/10.1007/BF00562002.pdf>
- Xie, M., Liu, T., & Xu, A. (2020). Ballistic sedimentation of impact crater ejecta: Implications for the provenance of lunar samples and the resurfacing effect of ejecta on the lunar surface. *Journal of Geophysical Research: Planets*, *125*(5). <Go to ISI>://WOS:000537906800009. <https://doi.org/10.1029/2019je006113>
- Xie, M., Xiao, Z., Zhang, X., & Xu, A. (2020). The provenance of regolith at the Chang'e-5 candidate landing region. *Journal of Geophysical Research: Planets*, *125*(5), e2019JE006112. <Go to ISI>://WOS:000537906800013. <https://doi.org/10.1029/2019je006112>
- Xu, J., Wang, M., Lin, H., Xu, X., Liu, B., Yan, W., et al. (2022). In-situ photometric properties of lunar regolith revealed by lunar mineralogical spectrometer on board Chang'E-5 lander. *Geophysical Research Letters*, *49*(4), e2021GL096876. <Go to ISI>://WOS:000765659300093. <https://doi.org/10.1029/2021gl096876>
- Yang, M. (2023). Mineralogy of surface materials at the Chang'E-5 landing site and possible exotic sources from in-situ spectral observations [Dataset]. Zenodo. <https://doi.org/10.5281/zenodo.8396087>
- Yang, W., Chen, Y., Wang, H., Tian, H.-C., Hui, H., Xiao, Z., et al. (2022). Geochemistry of impact glasses in the Chang'E-5 regolith: Constraints on impact melting and the petrogenesis of local basalt. *Geochimica et Cosmochimica Acta*, *335*, 183–196. <Go to ISI>://WOS:000862791900001. <https://doi.org/10.1016/j.gca.2022.08.030>
- Zeng, X., Li, X., & Liu, J. (2023). Exotic clasts in Chang'e-5 regolith indicative of unexplored terrane on the Moon. *Nature Astronomy*, *7*(2), 152–159.
- Zhang, H., Yang, Y., Yuan, Y., Jin, W., Lucey, P. G., Zhu, M. H., et al. (2015). In situ optical measurements of Chang'E-3 landing site in mare Imbrium: 1. Mineral abundances inferred from spectral reflectance. *Geophysical Research Letters*, *42*(17), 6945–6950. <Go to ISI>://WOS:000363411200010. <https://doi.org/10.1002/2015gl065273>
- Zhang, H., Zhang, X., Zhang, G., Dong, K., Deng, X., Gao, X., et al. (2021). Size, morphology, and composition of lunar samples returned by Chang'E-5 mission. *Science China Physics, Mechanics & Astronomy*, *65*(2), 229511. <https://doi.org/10.1007/s11433-021-1818-1>
- Zhou, C., Jia, Y., Liu, J., Li, H., Fan, Y., Zhang, Z., et al. (2022). Scientific objectives and payloads of the lunar sample return mission—Chang'E-5. *Advances in Space Research*, *69*(1), 823–836. <https://doi.org/10.1016/j.asr.2021.09.001>